Applied Science and Engineering Progress, Vol. 20, No. 2, 2026, 8262

Research Article

Green Synthesis of Plant Mediated-Based MnO_2 Electrocatalysts Using *Clerodendrum infortunatum* L. for Enhanced Oxygen Reduction and Evolution in Solid-Electrolyte Zinc-Air Batteries

Manat Jaimasith * and Wanrudee Kaewmesri
Division of Chemistry, School of Science, University of Phayao, Phayao, Thailand

Arrak Klinbumrung
Division of Physics, School of Science, University of Phayao, Phayao, Thailand

* Corresponding author. E-mail: manat.ja@up.ac.th
DOI:10.14416/j.asep.2026.08.006
Received: 21 March 2026; Revised: 16 May 2026; Accepted: 21 July 2026; Published online: 17 August 2026

Abstract
This study investigated the green synthesis of MnO_2-based electrocatalysts using *Clerodendrum infortunatum* L. flower and leaf extracts as natural reducing and capping agents via a comproportionating reaction. Bioactive compounds facilitated Mn^{7+} to Mn^{4+} reduction and stabilized the resulting flower-mediated (FM) and leaf-mediated (LM) composites. Characterization via UV–Visible spectroscopy, XRD, and SEM-EDS confirmed aggregated nanoparticle clusters (50–200 nm) with uniform Mn, O, and C distribution. High carbon content confirmed MnO_2–organic carbon composite formation, which improved electrical conductivity and structural stability. The composites were fabricated into electrodes (FME and LME) and evaluated as air cathodes for solid-electrolyte zinc–air batteries. Both exhibited Oxygen Evolution Reaction (OER) performance comparable to commercial Pt/C (onset potentials: 1.5–1.6 V; overpotentials: 450–460 mV). For Oxygen Reduction Reaction (ORR), onset potentials of 0.7–0.8 V vs. RHE were recorded, with steeper slopes than Pt/C, indicating superior kinetics. Batteries discharged at 2 mA/cm² showed that FME delivered a discharge capacity of 6.00 mAh/cm², approximately 9 times that of Pt/C (0.63 mAh/cm²), while maintaining 1.05 V over 180 minutes. The utilization of plant extracts as natural reducing agents in the green synthesis approach offers a promising and environmentally responsible alternative for the fabrication of electrocatalysts in next-generation zinc-air battery applications, although a comprehensive techno-economic analysis remains necessary to fully validate its potential economic advantages.

Keywords: *Clerodendrum infortunatum* L., Electrocatalyst, Green synthesis, Manganese dioxide, Oxygen reduction reaction, Phytochemicals, Solid-electrolyte zinc–air battery

1 Introduction

Global energy demand increased rapidly due to population growth and industrial expansion. As a result, non-renewable energy sources, such as coal, oil, and natural gas, decreased steadily. Furthermore, the use of fossil fuels was a major cause of greenhouse gas emissions, which significantly affected the global environment. According to the World Health Organization (WHO), pollution and climate change cause 160,000 deaths per year [1]-[3], resulting in higher greenhouse gas emissions and severe climate change. In response, a global target is set to reduce emissions by 45% by 2030, aiming for Net Zero by 2050 [4]. Meeting this target requires developing clean energy sources to replace fossil fuels [5]-[7].

Metal-air batteries are a promising technology for the clean energy transition, particularly for electric vehicles (EVs) and energy storage systems. They offer several advantages, including high energy density, light weight, low cost, and low environmental impact [8]-[10]. However, these batteries face a critical limitation: the oxygen reduction reaction (ORR) during discharge and the oxygen evolution reaction (OER) during charge are inherently difficult to achieve due to the high energy required to break O=O bonds. The sluggish kinetics of these reactions lead to large overpotentials, which significantly reduce overall energy efficiency [11]-[15].

Table 1 compares four major electrocatalyst strategies for zinc–air batteries based on materials and performance. Noble metal catalysts, including Pt, Ru, and Ir, delivered fast reaction kinetics but were prohibitively expensive for large-scale application [16]-[18], [19]-[20]. Carbon-based materials, such as carbon black and activated carbon, offered a cost-effective alternative with high porosity; however, they were susceptible to oxidation in alkaline environments [21]. Lignin-based nanocomposites valorized biomass waste and generated highly active catalytic sites, although they required energy-intensive high-temperature pyrolysis [22],[23]. Plant-mediated nanoparticle synthesis emerged as the most promising approach, utilizing natural plant extracts to produce catalysts with diverse morphologies at low cost [24]. However, it often requires the incorporation of additional carbon supports to improve catalyst stability and performance.

Transition metal-based catalysts, specifically those using earth-abundant metals like Fe, Co, Ni, Mn, and Cu, attracted considerable interest. These metals were incorporated into various forms, such as alloys, oxides, and nitrides, offering diverse options for catalyst design [25]-[27]. MnO_2 is a transition metal-based catalyst with significant potential. It exhibits catalytic activity comparable to Pt while being non-toxic, eco-friendly, and inexpensive. MnO_2 presents various morphologies that influence performance. Although methods like hydrothermal or sonochemical reduction exist, they often involve limitations such as high pressure, long processing times, and environmental concerns [28]-[30], [31]-[32].

Green synthesis refers to an environmentally benign approach that employs plant extracts as reducing and stabilizing agents, eliminating the need for toxic chemicals and high energy processes. The mechanism of green synthesis using plant extracts was conducted through a sustainable bottom-up approach, involving three primary stages: activation, nucleation, and growth. During the activation phase, phytochemicals utilized functional groups with high reducing potential, such as hydroxyl (-OH), carbonyl (-C=O), and carboxyl (-COOH), which served as reducing agents by donating electrons or hydrogen ions to reduce metal ions into neutral atoms. As the process transitioned into the growth phase, these atoms aggregated into larger nanoparticles and achieved a complete zero-valent state. Simultaneously, biomolecules such as proteins and flavonoids, featuring functional groups including carbonyl (-C=O) and amines ($-NH_2$), acted as capping and stabilizing agents. These molecules adhered to the nanoparticle surfaces through coordinate bonds or electrostatic forces, which effectively prevented particle agglomeration and regulated the final morphology of the synthesized nanostructures [33]-[35].

The phytochemicals present in plant extracts exhibited notable biological properties and showed promising potential in materials science. Beyond their medicinal applications, these compounds served as reducing agents in green synthesis, reducing environmental impacts. Green synthesis offers a scalable, cost-effective, safer alternative to hazardous chemicals conventionally used in the production of metallic nanoparticles [36]-[38].

Plants are valuable sources of bioactive compounds; specifically, flavonoids and polyphenols in plant extracts act as effective reducing agents due to their availability and safety.

Table 1: Comparison of electrocatalyst strategies for Zinc–Air batteries.

Strategy	Matrices	Advance	Limitation
Plant mediated nanoparticle synthesis	Plant extracts (e.g., *Calpurnia aurea*, breadfruit juice), manganese salts.	Low cost and environmental friendliness; diverse morphologies provide high surface area and multiple valence states for catalytic activity [16],[24].	Low conductivity usually requires additional carbon supports. Susceptible to phase transformation or dissolution over extended cycles [16],[24].
Nanolignin based composites	Lignin, transition metals (Fe, Co, Ru), nitrogen sources (DCDA), sacrificial templates (Mg acetate)	Forms stable, highly active $M-N_x-C$ sites (e.g., Fe-N-C). Highly conductive graphitic carbon after pyrolysis. Valorizes abundant biomass waste [22], [23].	Requires high-temperature pyrolysis (800–1000 °C). Lignin's complex structure complicates quality control [22], [23].
Carbon black or activated carbon	Wood, agricultural waste, coconut shells, or commercial carbon [21].	Excellent porosity facilitates rapid gas/ion transport. Extremely cheap, accessible, and scalable for industrial use. Facile surface functionalization with heteroatoms [21].	Carbon is prone to oxidation in harsh alkaline/oxidative environments, weakening the electrode. Requires extensive doping (N, S, P) to achieve high catalytic activity [21].
Noble metal catalyst	Platinum (Pt), Ruthenium (Ru), or Iridium (Ir) on carbon supports [16],[17].	Currently the "gold standard" for fast ORR (Pt) and OER (Ru/Ir) kinetics. High half-wave potentials ($E_{1/2}$) [17].	Extremely high cost and limited natural abundance. Rarely performs both ORR and OER efficiently in a single material. Sensitive to methanol and CO [17].

Research on *Clerodendrum infortunatum* L. (Hill Glory Bower) confirms that its roots, leaves, and flowers contain diverse phytochemicals, including saponins, tannins, and phenolic acids. The concentration of these compounds varies based on plant age and growing conditions [39]-[41].

In this regard, the synthesis of MnO_2 using plant extracts attracted growing interest as an environmentally friendly approach. However, most existing studies were limited to demonstrating the feasibility of the synthesis process, and the application of plant-mediated MnO_2 as an electrocatalyst for the oxygen reduction reaction (ORR) and oxygen evolution reaction (OER) was not yet reported. Moreover, comparative investigations on the influence of extracts derived from different plant parts, such as flowers and leaves, on the structural and electrochemical properties of the synthesized MnO_2 remained largely unexplored. Importantly, *Clerodendrum infortunatum* L. was not previously explored as a biological source for green synthesis. To address these gaps, this study aims to employ extracts from the flowers and leaves of *Clerodendrum infortunatum* L. for the synthesis of MnO_2 and to evaluate its electrocatalytic performance at the cathode of solid-electrolyte zinc–air batteries. The synthesized catalysts will be assessed in both half-cell and full-cell configurations, with the aim of developing a cost-effective alternative to conventional ORR catalysts.

2 Materials and Methods

2.1 *Preparation of plant extracts and synthesis of MnO_2-C nanocomposite*

Plant extracts were prepared from *Clerodendrum infortunatum* L. flowers and leaves collected from Mueang District, Phayao Province, Thailand (19.247896, 99.827856). The raw materials were washed thoroughly with tap water, dried in a hot-air oven at 50°C, and ground in a ceramic mortar to a particle size below 20 mesh. The powders were extracted by boiling with deionized water at 60°C for 1 hour (5 g per 100 mL). The solutions were filtered to obtain flower and leaf extracts.

The LM sample was synthesized by mixing 5 mL of leaf extract with 25 mL of 0.05 M MnSO4, then adding the mixture dropwise to 25 mL of 0.05 M KMnO4 under continuous stirring (120 rpm) at room temperature for 1 hour. The color change from purple to dark brown indicated a complete reaction. The precipitate was separated by centrifugation (5,000 rpm), washed three times with deionized water, and dried via freeze-drying. The FM sample was prepared using the same procedure as the flower extract.

2.2 *UV–visible spectroscopy analysis*

The optical properties were investigated using a Jasco V-530 UV/Vis spectrophotometer. Absorption spectra of the extracts, nanoparticles, and reaction mixtures were recorded from 200 to 800 nm, using deionized water as the baseline.

2.3 *XRD analysis*

The crystalline structures of LM and FM were examined using a Rigaku Smart Lab X-ray diffractometer (CuKα radiation, λ = 1.54056 Å) at 9 kV. Diffraction patterns were collected over a 2θ range of 10°–80° with 0.02° steps [31].

2.4 *Photoluminescence analysis*

The MnO_2-C nanocomposite, LM and FM, were prepared for Photoluminescence (PL) analysis. Each dried sample was ground into a fine and uniform powder using a mortar and pestle to improve material homogeneity and minimize light scattering during measurement. The powder was then placed into a sample holder and pressed to obtain a flat and smooth surface. The prepared samples were analysed using a Photoluminescence Spectrometer (Jasco, model FP-8350) to investigate charge separation and transfer behaviour. An excitation wavelength of 370 nm was used, and the emission spectra were recorded over 400-700 nm at room temperature. The PL intensity of LM and FM was compared and used as an indicator of the electron-hole recombination rate within the nanocomposite material structure [29],[42].

2.5 *SEM EDS analysis*

Surface morphology and elemental dispersion were analysed using a Hitachi SU3800 scanning electron microscope. The MnO_2-C nanocomposite, LM and FM, were sputter-coated with gold prior to imaging to enhance conductivity [31].

Applied Science and Engineering Progress, Vol. 19, No. 4, 2026, 8122

2.6 *Air electrodes fabrication*

LM powder was ground to a size below 200 mesh. Then, 0.0100 g of the sample was mixed with 900 µL of absolute methanol and 100 µL of Nafion solution [43],[44]. The mixture was homogenized in an ultrasonic bath for 10 minutes. The resulting suspension was spray-coated onto a gas diffusion layer (GDL) at a loading of 2 mg/cm² and dried at 60°C for 30 minutes to form the LME electrode. FME and Pt/C electrodes were prepared using the same protocol.

2.7 *Electrochemical measurements*

Electrochemical measurements were performed using a Squidstat Plus potentiostat in a three-electrode configuration. The working electrodes (LME, FME, or Pt/C) were coated onto a GDL (0.25 cm² active area). A saturated calomel electrode (SCE) and a platinum plate served as the reference and counter electrodes, respectively. All the recorded potentials were then calibrated vs. the reversible hydrogen electrode (RHE) through the following Nernst equation:

$$E_{RHE} = E_{SCE} + 0.241V + 0.0592 \times pH \quad (1)$$

where ERHE is the converted potential vs. RHE, and ESCE is the experiment record.

All tests were conducted in 1 M KOH. The electrolyte was purged with N_2 or O_2 for 45 minutes before each measurement. Linear-sweep voltammetry (LSV) was performed at 10 mV/s. The potential windows were set to 1.0–2.2 V vs. RHE for OER and 1.3–0.0 V vs. RHE for ORR. Cyclic voltammetry (CV) was performed at 200 mV/s from 0.4 to 2.2 V vs. RHE to assess stability [25],[30].

2.8 *Solid-electrolyte zinc-air battery assembly and discharge testing*

Homemade solid-electrolyte zinc–air batteries were assembled using a pure zinc sheet as the anode. Three types of air cathodes—LME, FME, and Pt/C—were selected for comparison of their discharge performance, with Pt/C serving as the benchmark for ORR activity. The solid electrolyte consisted of a PVA/PVP film cross-linked with glutaraldehyde (250 µm thickness), chosen for its mechanical flexibility and chemical stability. Before assembly, the film was soaked in 6 M KOH for 24 hours to ensure adequate ionic conductivity through the polymer matrix.

Cell assembly was carried out by stacking the components in a defined sequence: a pure zinc sheet anode at the bottom, followed by the KOH-soaked electrolyte, the air cathode, and a stainless-steel mesh current collector. The entire stack was sandwiched between air-perforated plastic plates to prevent short circuits while allowing air to pass. The assembly was secured with metal clips to maintain uniform contact pressure and minimize interfacial resistance. Each cell was allowed to rest at room temperature for 1 hour to reach electrochemical equilibrium before testing.

Discharge performance was evaluated using a Newware battery tester model CT-4008Tn-5V6A S1. All cells were discharged at a constant current density of 2 mA/cm². The discharge process was terminated when the cell voltage dropped below the cutoff of 0.4 V. Finally, the discharge profiles from each cell were analysed and compared.

3 Results and Discussion

3.1 *UV–visible spectroscopy*

The study measured and compared the light absorbance of several solutions, including extracts from *Clerodendrum infortunatum* L. leaves and flowers, precursor solutions of $KMnO_4$ and $MnSO_4$, and the supernatant remaining after the green synthesis of MnO_2 nanoparticles. During synthesis, the formation of MnO_2 was visually observable as the purple $KMnO_4$ solution gradually transformed into a dark brown-black suspension. This change indicated the reduction of Mn^{7+} to Mn^{4+}, facilitated by bioactive compounds in the plant extracts acting as reducing agents. To confirm these changes, the absorbance of each solution was measured using a UV-Visible spectrophotometer over 200-800 nm.

As shown in Figure 1, the leaf extract gave a yellowish-brown solution with an absorbance range of 200–450 nm. This range was consistent with the characteristics of phenolic compounds and flavonoids, which served as reducing agents by donating electrons or hydrogen to $KMnO_4$ [37],[39]. The post-synthesis supernatant was colourless, with a significant decrease in absorbance at 235 nm and beyond, suggesting that the bioactive compounds were consumed during the reaction.

In contrast, the flower extract produced a dark reddish-brown solution with a broader absorbance spectrum (200–800 nm) and a distinct peak at 430 nm. This peak was attributed to anthocyanins, carotenoids, or other phenolic substances [37],[39].

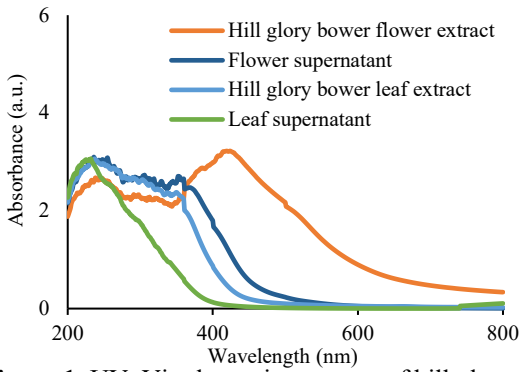

Figure 1: UV–Vis absorption spectra of hill glory.

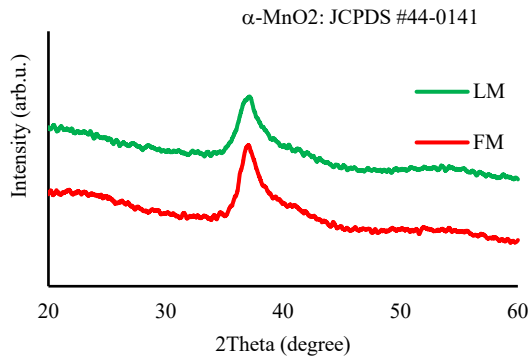

Figure 2: XRD pattern of LM and FM.

The broader spectral profile indicated a greater variety of bioactive compounds compared to the leaf extract. Following synthesis, a significant decrease in absorbance was observed between 370 and 800 nm, confirming that these compounds participated in the reduction process.

These findings demonstrated that the bioactive compounds involved in the synthesis differed in both type and quantity between the leaf and flower extracts. The leaf extract contained compounds absorbing at shorter wavelengths, while the flower extract possessed a more diverse range covering a broader spectrum. These variations in reducing and capping agents likely resulted in MnO_2 nanoparticles with distinct physical and chemical properties, including size, morphology, and catalytic activity, warranting further investigation.

3.2 *XRD analysis*

Figure 2 shows the XRD patterns of the two synthesized particles, LM and FM. The diffraction peaks of both materials appeared broad and low in intensity, indicating low crystallinity or composite characteristics. This result was consistent with the EDS elemental analysis, which revealed a high carbon content of approximately 63–64 % atomic. Furthermore, the MnO_2 crystallite size was at the nanoscale, which contributed to a high surface area and was beneficial for electrocatalytic activity. The XRD pattern showed a main peak at $2\theta = 37°$, which corresponded to the (211) crystal plane of α-MnO_2 according to the JCPDS #44-0141 standard [45]. This confirmed that both materials exhibited an alpha-phase manganese dioxide (α-MnO_2) structure.

3.3 *Photoluminescence analysis*

The optical properties of two carbon-MnO_2 nanocomposite materials, LM and FM, were investigated using both steady-state and time-resolved photoluminescence (PL) techniques.

The optical properties of two carbon-MnO_2 nanocomposite materials, LM and FM, were investigated using both steady-state and time-resolved photoluminescence (PL) techniques. The PL spectra recorded in the wavelength range of 400–700 nm in Figure 3 showed that FM exhibited significantly lower PL intensity than LM. This quenching phenomenon confirmed that FM had a lower electron-hole recombination rate, allowing excited electrons sufficient time to migrate to the catalyst surface and undergo redox reactions with oxygen more effectively [43]. As a result, FM demonstrated higher current output and a higher product generation rate while reducing heat loss due to recombination. Furthermore, during the discharge process involving the oxygen reduction reaction, ORR, the lower electron-hole recombination in FM enabled electrons from the anode to react directly with oxygen at the cathode surface without significant energy loss. This reduced the overpotential and led to a higher, more stable working voltage, both desirable characteristics for an electrocatalytic material.

The PL decay dynamics curves in Figure 4 showed that both samples exhibited similar behaviour during the initial period, during which the signal remained stable up to approximately 45 ms. However, a clear difference was observed between 45 and 55 ms, where FM showed a more abrupt, steeper signal decay with a shorter resolved time. This indicated that FM had superior charge-transfer efficiency, as excited electrons in MnO_2 migrated into the carbon framework, which served as an electrical conductor, more rapidly.

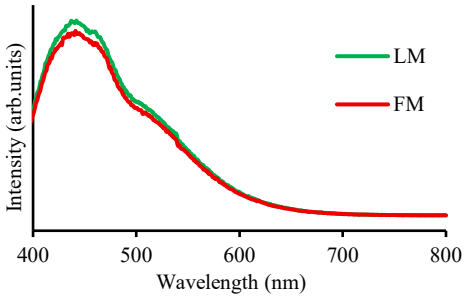

Figure 3: Photoluminescence spectra of LM and FM nanoparticles.

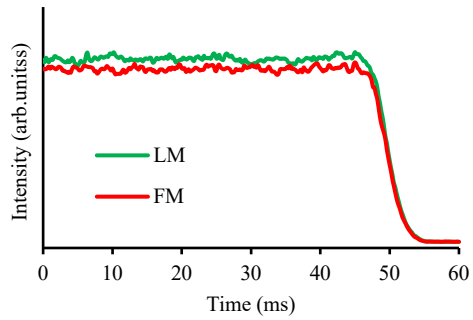

Figure 4: Photoluminescence decay dynamics curves of LM and FM nanoparticles.

These results demonstrated that FM provided better interfacial contact between carbon and MnO_2, thereby improving charge separation and electron transfer efficiency while reducing energy loss due to internal resistance. Overall, both analyses confirmed that FM exhibited higher electrocatalytic activity than LM.

3.4 *SEM and EDS analysis*

The morphology and chemical composition of LM and FM particles were investigated using SEM and EDS techniques. Table 2 summarizes the elemental composition obtained from EDS mapping. The atomic ratio of Mn to O was approximately 1:2, which aligned with the stoichiometry of MnO_2. Furthermore, the carbon content was recorded as high as 63–64%, suggesting that the synthesized products consisted of MnO_2 combined with organic carbon compounds derived from the plant extracts, such as polyphenols and flavonoids. These compounds acted as both reducing and stabilizing agents during the synthesis. It was also evident that these carbonaceous species coated the MnO_2 surfaces, serving as binders that promoted particle aggregation into a composite material.

Table 2: The elemental composition of LM and FM nanoparticles.

	Atomic%	
Element	LM	FM
C	64.35	63.42
O	24.70	24.69
Mn	10.95	11.89
Total	100.00	100.00

The aggregation of MnO_2 nanoparticles was confirmed by the secondary electron images in Figure 5, where the clusters ranged from 50 to 200 nm. Such nanometre-scale dimensions were considered ideal for electrode applications, as the high specific surface area facilitated efficient electrochemical reactions. This nanocomposite structure offered distinct advantages in electrical connectivity; the carbon coating enhanced conductivity and reduced internal resistance. This reduction minimized energy losses during battery discharge, especially under high-power conditions. Additionally, the composite structure improved the structural stability of the material during operation, which was a critical factor for cycle life.

EDS mapping results in Figure 6 show that manganese, oxygen, and carbon were uniformly distributed throughout the samples, indicating a homogeneous product. This uniform distribution confirmed that both leaf and flower extracts of *Clerodendrum infortunatum* L. were effective in producing high-quality MnO_2-organic carbon nanocomposites. Consequently, these materials demonstrated significant potential for use as air electrodes in zinc–air batteries.

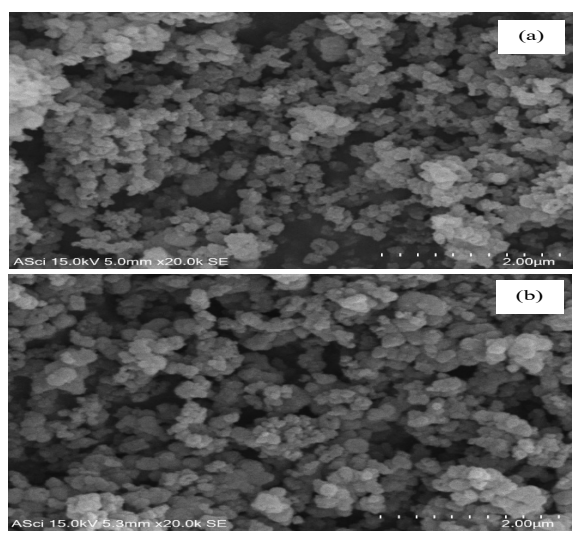

Figure 5: Secondary electron image of (a) LM and (b) FM nanoparticle at 20,000x.

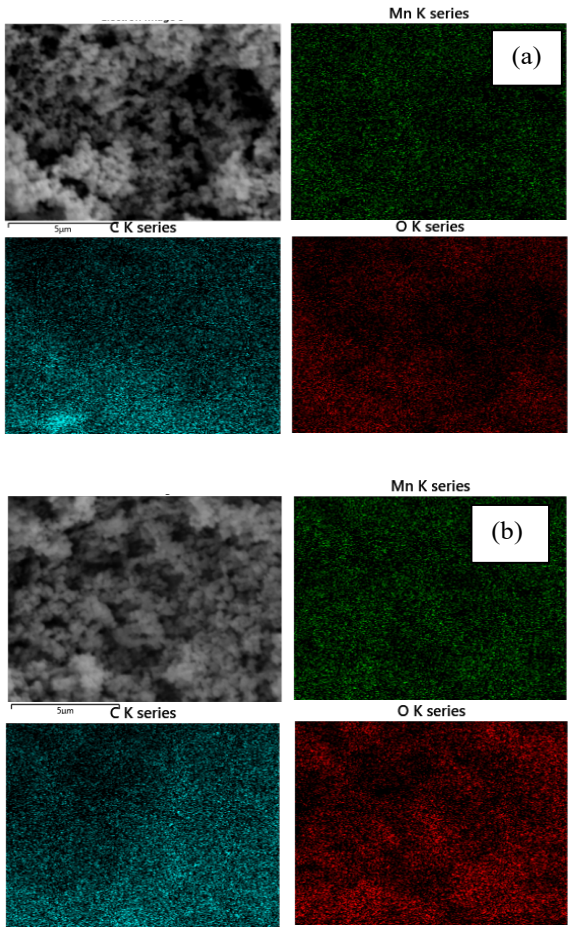

Figure 6: EDS element mapping image of (a) LM and (b) FM nanoparticle at 20,000x.

3.5 *Electrochemical properties of air electrodes in a half-cell*

3.5.1 Oxygen evolution reaction (OER) electrocatalyst tests

The Oxygen Evolution Reaction (OER) occurred during the charging process, where hydroxide ions underwent oxidation to produce oxygen and water. Due to its complex four-electron transfer mechanism and high activation energy, an overpotential was required to drive the reaction. Figure 7 presents the Linear Sweep Voltammetry (LSV) results in 1 M KOH, which was purged with nitrogen for 45 minutes prior to testing. The potential was scanned from 1.0 to 2.2 V vs. RHE to evaluate the onset potential and overpotential of each electrode [6],[7]. The results showed that LME, FME, and Pt/C exhibited

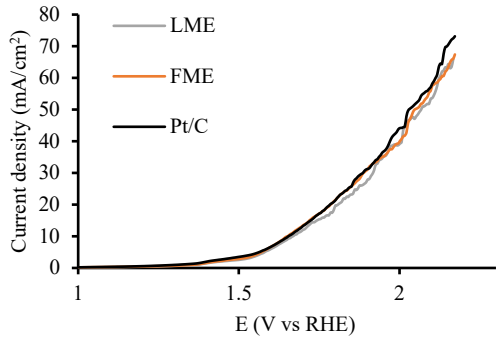

Figure 7: The linear sweep voltammetry (LSV) curves for the oxygen evolution reaction (OER) of the air electrode.

comparable onset potentials (1.5–1.6 V) and overpotentials (450–460 mV). These findings indicated that the bio-synthesized LME and FME possessed charging capabilities similar to those of the high-cost Pt/C benchmark. Notably, noise signals were observed in the LSV curves, likely originating from the partial detachment of the catalyst layer. The high current density during testing may have weakened adhesion between the catalyst and the electrode surface, leading to delamination.

3.5.2 Oxygen reduction reaction (ORR) electrocatalyst tests

The Oxygen Reduction Reaction (ORR) performance was evaluated to determine the discharge capability of the air electrodes. Figure 8 displayed the LSV curves in oxygen-saturated 1 M KOH over a potential range of 0–1.3 V vs. RHE. The Pt/C electrode exhibited an onset potential of 0.9 V, which was higher than those of LME and FME (0.7–0.8 V).

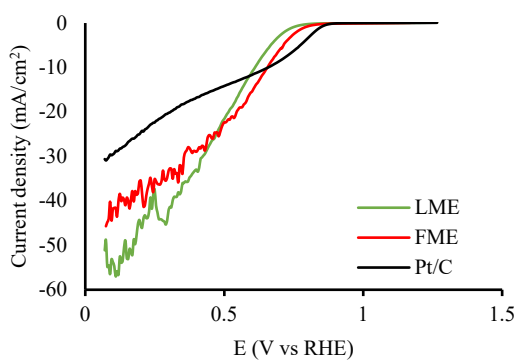

Figure 8: The linear sweep voltammetry (LSV) curves for the oxygen reduction reaction (ORR) of the air electrode.

This indicated that Pt/C initiated the ORR at a lower overpotential due to its superior oxygen adsorption.

However, both LME and FME demonstrated significantly steeper current density slopes than Pt/C, suggesting more rapid reaction kinetics as the voltage decreased. This indicated that cells incorporating LME or FME had the potential to deliver higher current under load conditions. Despite the cost advantages of LME and FME, their LSV profiles appeared notably noisy, which was attributed to catalyst delamination at high current densities. These observations suggested that further optimization of the electrode coating technique, such as surface pretreatment or binder adjustment, was required to enhance long-term stability.

3.5.3 Cyclic voltammetry

Figure 9 shows the electrochemical properties of Pt/C, FME, and LME catalysts measured by Cyclic Voltammetry (CV) over a potential range of 0.4–2.1 V vs. RHE at a scan rate of 200 mV/s [4],[5]. In the first cycle, Pt/C delivered the highest current density. However, after 20 cycles, the current density decreased significantly, indicating the limited durability of Pt/C, which may have resulted from platinum dissolution or carbon degradation

In contrast, although FME and LME exhibited higher onset potentials than Pt/C, both catalysts demonstrated better electrochemical stability. No significant decrease in current density was observed after 20 cycles. FME showed stable redox peaks and higher current density than LME, suggesting a more durable structure and superior long-term catalytic performance

3.6 *Zn-air cell assembly and discharge testing*

Figure 10 presents the discharge curves of the solid-electrolyte zinc–air batteries fabricated with LME, FME, and Pt/C air electrodes. This test evaluated the actual performance of the assembled batteries under a continuous current density of 2 mA/cm². Prior to discharge, the Open Circuit Voltage (OCV) was monitored for 30 minutes to reach electrochemical equilibrium. The OCV measurements revealed that batteries using LME, FME, and Pt/C exhibited values of 1.44 V, 1.56 V, and 1.38 V, respectively. The FME-based battery demonstrated the highest OCV, indicating superior electrochemical potential, while the Pt/C-based battery showed the lowest.

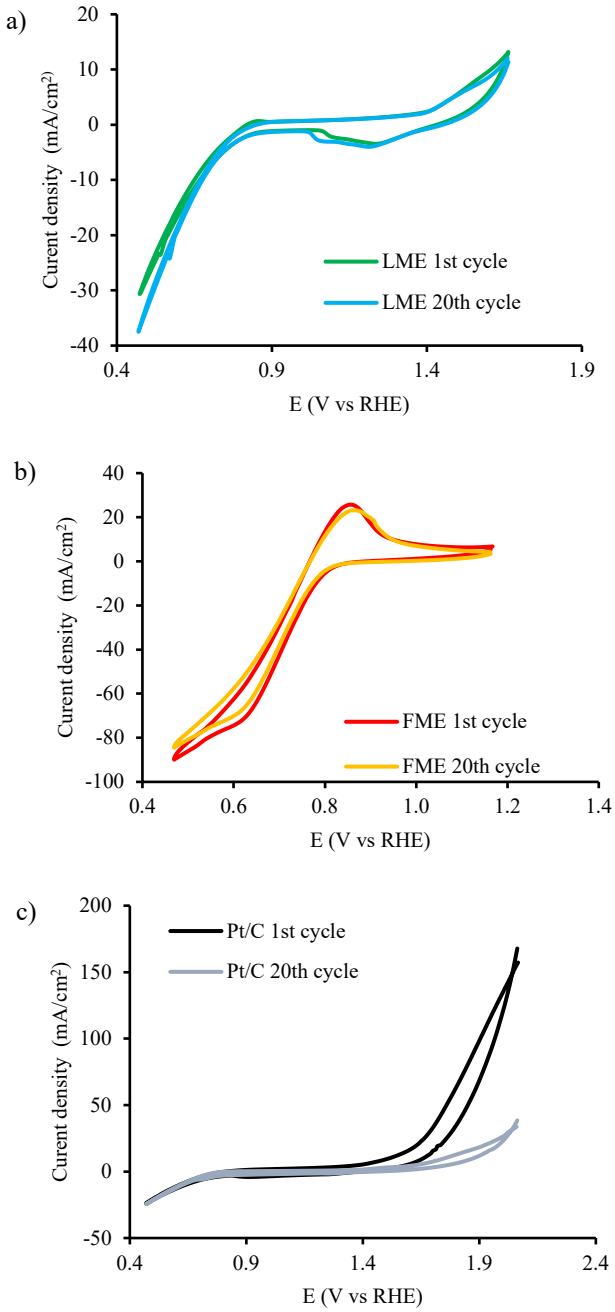

Figure 9: The cyclic voltammetry (CV) curves for the stability assessment of the air electrode (a) LME, (b) FME, and (c) Pt/C.

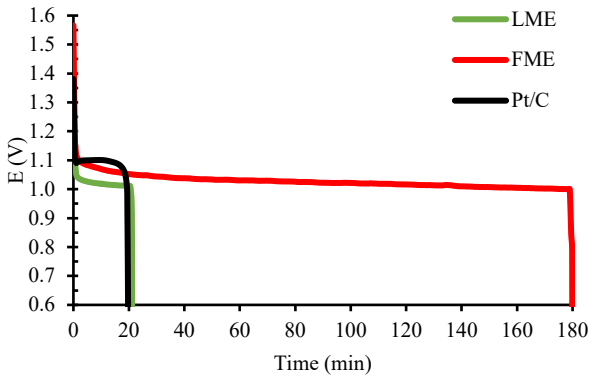

Figure 10: Zn-air battery discharge curve.

During discharge, the Pt/C battery maintained a stable voltage of 1.1 V for 19 minutes before a rapid decline, yielding a capacity of 0.63 mAh/cm². Similarly, the LME battery sustained 1.02 V for 23 minutes, delivering a capacity of 0.76 mAh/cm². These rapid voltage drops were attributed to zinc anode depletion or the accumulation of reaction products. In contrast, the FME battery demonstrated significantly superior performance, maintaining a stable discharge voltage of 1.05 V for 180 minutes.

The resulting capacity was 6.0 mAh/cm², approximately nine times higher than that of the Pt/C and LME batteries. These findings indicated that FME contained substantially greater discharge durability and ORR catalytic activity than the other electrodes. The outstanding performance was potentially attributed to the bioactive compounds from *C. infortunatum* L., which formed a nanocomposite with MnO_2. This composite structure likely enhanced performance by reducing internal resistance, protecting active sites from degradation, and increasing the effective active surface area.

Compared with the commercial Pt/C catalyst, the FME exhibits superior ORR/OER performance and discharge capacity in the solid-state Zn–air battery, which can be attributed to both intrinsic material properties and electrode–electrolyte interactions. Although Pt/C is widely regarded as a benchmark ORR catalyst, its performance in the present solid-electrolyte configuration is limited by poor interfacial compatibility and less favourable mass and charge transport under alkaline solid-electrolyte conditions.

In contrast, the plant-mediated MnO_2 catalysts possess abundant surface defects, oxygen vacancies, and residual bio-derived carbon species, which facilitate hydroxide ion adsorption, intermediate stabilization, and electron transfer during oxygen electrocatalysis. Moreover, the hydrophilic surface functional groups derived from phytochemicals enhance electrode wettability and ionic accessibility, leading to more effective utilization of active sites. These results indicate that, while Pt/C remains effective in conventional liquid electrolyte systems, green-synthesized FME offers clear advantages in solid-electrolyte Zn–air batteries, highlighting its potential as a sustainable and cost-effective alternative to noble metal catalysts.

4 Conclusions

This study focuses on the green synthesis of manganese dioxide (MnO_2) nanocomposites using extracts from the leaves and flowers of *Clerodendrum infortunatum* L. The extracts contain bioactive compounds that function as both reducing and capping agents, facilitating the formation and stabilization of MnO_2 nanoparticles. These synthesized materials are applied as air-cathode catalysts for solid-electrolyte zinc–air batteries, aiming to provide a high-performance, low-cost, and eco-friendly alternative to conventional noble-metal catalysts.

The results show that both extract types successfully produce MnO_2 nanocomposites. The resulting products are nanocomposite materials comprising MnO_2 and carbonaceous/organic components derived from plant extracts. This composite nature enhances surface characteristics and charge-transfer behaviour, which are crucial for electrochemical oxygen reactions. The catalysts, denoted as LME and FME, exhibited oxygen evolution reaction (OER) activity comparable to that of a Pt/C air cathode. In contrast, their oxygen reduction reaction (ORR) performance was superior to that of Pt/C, with the FME-based cathode demonstrating the strongest ORR activity, as evidenced by more effective reaction kinetics and greater electrochemical durability.

In solid-electrolyte zinc–air battery cells, the FME air cathode delivers a discharge capacity approximately 9 times that of Pt/C. These findings demonstrate that green-synthesized MnO_2 nanocomposites, particularly FME, are highly suitable for primary solid-electrolyte zinc–air batteries due to their superior performance and sustainable synthesis route.

However, the material is not yet ideal for rechargeable systems, as its OER catalytic activity remains insufficient for efficient charging, resulting in increased overpotential and energy loss. Therefore, further improvement of OER activity through structural optimization is necessary to enable effective rechargeable operation.

Acknowledgments

This research was supported by University of Phayao and Thailand Science Research and Innovation Fund (Fundamental Fund 2025, Grant No. 5121/2567). Additional supported by Chiang Mai University and Thailand Science Research and Innovation (TSRI) (Fundamental Fund 2026 Grant No. 214515) and (FRB690042/0162). The authors gratefully acknowledge this funding support, which played a pivotal role in facilitating and driving the successful completion of this research work.

Author Contributions

M.J.: Conceptualization, investigation, reviewing methodology, methodology, data curation and analysis, writing an original draft. W.K.: Data curation, editing. A.K.: XRD, PL data analysis editing. All authors have read and agreed to the published version of the manuscript.

Conflicts of Interest

The authors declare no conflict of interest.

Declaration of generative AI and AI-assisted technologies in the writing process

The authors utilized the AI tool to enhance the language and readability of the manuscript.

References

[1] M. A. Alemu, D. T. Ebissa, M. Z. Getie, A. K. Worku, H. M. Wassie, and M. S. Alem, "Recent development of rechargeable solid-state metal-air batteries for electric mobility," Energy Reports, vol. 12, pp. 517–528, Dec. 2024, doi: 10.1016/j.egyr.2024.06.007.

[2] B. Saha, P. M. Yunus, M. Khwairakpam, and A. S. Kalamdhad, "Biochemical methane potential trial of terrestrial weeds: Evolution of mono digestion and co-digestion on biogas production," *Materials Science for Energy Technologies*, vol. 3, pp. 748–755, 2020, doi: 10.1016/j.mset.2020.09.003.

[3] B. Saha, S. Koley, M. Khwairakpam, and A. S. Kalamdhad, "Comparative study between mono-digestion and co-digestion of terrestrial weed (Parthenium hysterophorus)," *Cleaner Engineering and Technology*, vol. 11, Art. no. 100560, Dec. 2022, doi: 10.1016/j.clet.2022 .100560.

[4] F. M. B. Gusmão et al.,"Transition metal polyoxometalates with reduced graphene oxide for high-performance air-electrode of metal-air batteries," *International Journal of Hydrogen Energy*, vol. 71, pp. 763–774, Jun. 2024, doi: 10.1016/j.ijhydene.2024.05 .229.

[5] J. Ahmed, M. Alam, M. A. M. Khan, and S. M. Alshehri, "Bifunctional electro-catalytic performances of NiMoO4-NRs@RGO nanocomposites for oxygen evolution and oxygen reduction reactions," *Journal of King Saud University – Science* (2020), vol. 33, no. 2, Art. no. 101317, Dec. 2020, doi: 2021, doi: 10.1016/j. jksus.2020.101317.

[6] C.-X. Zhao, B.-Q. Li, J.-N. Liu, and Q. Zhang, "Intrinsic electrocatalytic activity regulation of M-N-C single-atom catalysts for the oxygen reduction reaction," *Angewandte Chemie International Edition*, vol. 60, no. 9, pp. 4448–4463, Feb. 2021, doi: 10.1002/anie.2020039 17.

[7] A. K. Worku, D. W. Ayele, and N. G. Habtu, "Recent advances and future perspectives in engineering of bifunctional electrocatalysts for rechargeable zinc–air batteries," *Materials Today Advances*, vol. 9, Art. no. 100116, Mar. 2021, doi: 10.1016/j.mtadv.2020.100116.

[8] W. Tang et al., "Advanced noble-metal-free bifunctional electrocatalysts for metal-air batteries," *Journal of Materiomics*, vol. 8, no. 2, pp. 454–474, Mar. 2022, doi: 10.1016/j. jmat.2021.07.0.

[9] M. A. Alemu, A. K. Worku, and M. Z. Getie, "Recent advances in electrically rechargeable transition metal-based-air batteries for electric mobility," *Inorganic Chemistry Communications*, vol. 159, Art. no. 111742, Jan. 2024, doi: 10.1016/j.inoche.2023.111742.

[10] Q. Jin, L. Xiao, W. He, H. Cui, and C. Wang, "Self-supported metal (Fe, Co, Ni)-embedded

nitrogen-doping carbon nanorod framework as trifunctional electrode for flexible Zn-air batteries and switchable water electrolysis," *Green Energy & Environment*, vol. 8, no. 6, pp. 1644–1653, Dec. 2023, doi: 10.1016/j.gee.2022.03.008.

[11] P. Mishra, D. Singh, Y. Sonvane, and R. Ahuja, "Bifunctional catalytic activity of 2D boron monochalcogenides BX (X = S, Se, Te)," *Materials Today Energy*, vol. 27, Art. no. 101026, Jul. 2022, doi: 10.1016/j.mtener.2022. 101026.

[12] M. A. Alemu and A. A. Assegie, "Advancements in biomass-derived single-metal-doped nanostructured arbon electrocatalysts and electrode materials for rechargeable zinc-air batteries," *iScience*, vol. 29, no. 2, Art. no. 114677, Feb. 2026, doi: 10.1016/j.isci.2026.114677.

[13] L. Zhang, Q. Shao, and J. Zhang, "An overview of non-noble metal electrocatalysts and their associated air cathodes for Mg-air batteries," *Materials Reports: Energy*, vol. 1, no. 1, Art. no. 100002, Feb. 2021, doi: 10.1016/j.matre.2020.11.001.

[14] Y. Niu et al., "Engineering iron-group bimetallic nanotubes as efficient bifunctional oxygen electrocatalysts for flexible Zn–air batteries," *eScience*, vol. 2, no. 5, pp. 546–556, Oct. 2022, doi: 10.1016/j.esci.2022.05.001.

[15] M. Posadzy et al., "High-performance transition metal nitride/carbon nanofiber composites as positive electrode in rechargeable Zn-air batteries," *Carbon*, vol. 239, Art. no. 120308, Jun. 2025, doi: 10.1016/j.carbon.2025.120308.

[16] X. Yi, Y. Song, D. He, W. Li, A. Pan, and C. Han, "Constructing a high-performance bifunctional MnO2-based electrocatalyst towards applications in rechargeable zinc–air batteries," *Journal of Materials Chemistry A*, vol. 12, no. 43, pp. 29355–29382, Nov. 2024, doi: 10.1039/d4ta05182c.

[17] M. Ruan, J. Liu, P. Song, and W. Xu, "Meta-analysis of commercial Pt/C measurements for oxygen reduction reactions via data mining," *Chinese Journal of Catalysis*, vol. 43, no. 1, pp. 116–121, Jan. 2022, doi: 10.1016/S1872-2067(21)63854-8.

[18] S. Fajardo, C. M. Sánchez-Sánchez, P. Ocón, J. L. Rodríguez, and E. Pastor, "RETRACTED: Manganese enriched zeolitic imidazole framework-67 and doped reduced graphene oxide hybrid electrocatalyst applied in alkaline Zn-air battery," *Chemical Engineering Journal Advances*, vol. 25, Art. no. 100999, Feb. 2026, doi: 10.1016/j.ceja.2025.100999.

[19] C. Dong et al., "Manipulating oxygenate adsorption on N-doped carbon by coupling with CoSn alloy for bifunctional oxygen electrocatalyst," *Green Energy & Environment*, vol. 8, no. 5, pp. 1417–1428, Oct. 2023, doi: 10.1016/j.gee.2022.02.005.

[20] M. Gao, C. Li, R. Wang, S. Xiao, Z. Guo, and Y. Wang, "Noble metal catalysts for metal-air batteries: From nano-level to atom-level," *Next Materials*, vol. 2, Art. no. 100126, Apr. 2024, doi: 10.1016/j.nxmate.2024.100126.

[21] M. A. Alemu, A. A. Assegie, M. Ilbas, R. Al Afif, and M. Z. Getie, "Biomass-derived metal-free nanostructured carbon electrocatalysts for high-performance rechargeable zinc–air batteries," *Advanced Energy and Sustainability Research*, vol. 6, no. 2, Art. no. 2400414, Feb. 2025, doi: 10.1002/aesr.202400414.

[22] Z. Zhang, V. Terrasson, and E. Guénin, "Lignin nanoparticles and their nanocomposites," *Nanomaterials*, vol. 11, no. 5, Art. no. 1336, May 2021, doi: 10.3390/nano11051336.

[23] Z. Nie, Y. Liu, L. Yang, X. Wang, C. Xu, and C. Wang, "Engineering biomass into advanced carbon-based materials for Zn-air batteries," *Science China Material*s, vol. 68, no. 5, pp. 1509–1529, May 2025, doi: 10.1007/s40843-024-3297-2.

[24] T. Subramaniam, B. S. Krishnaveni, and S. Devaraj, "Tuning the surface oxygen vacancies of α-MnO2 to enhance the kinetics of ORR and OER," *Journal of Materials Science: Materials in Electronics*, vol. 35, no. 17, Art. no. 1184, Jun. 2024, doi: 10.1007/s10854-024-12971-0.

[25] K. Mishra, N. Devi, S. S. Siwal, and V. K. Thakur, "Insight perspective on the synthesis and morphological role of the noble and non-noble metal-based electrocatalyst in fuel cell application," *Applied Catalysis B: Environmental*, vol. 334, Art. no. 122820, Oct. 2023, doi: 10.1016/j.apcatb.2023.122820.

[26] N. N. Rosman et al., "Nanostructured transition metal-based electrocatalysts: A promising pathway in anion exchange membrane water electrolysis," *Materials Today Sustainability*,

vol. 31, Art. no. 101203, Sep. 2025, doi: 10.10 16/j.mtsust.2025.101203.

[27] K. A. Jannath and H. A. Saputra, "Transition metal-based electrocatalysts for alkaline oxygen evolution reaction: Developments, challenges, and perspectives," *Next Materials*, vol. 9, Art. no. 101164, Dec. 2025, doi: 10.1016/j.nxmate. 2025.101164.

[28] F. Wang et al., "A critical review of facets and defects in different MnO2 crystalline phases and controlled synthesis – Its properties and applications in the energy field," *Coordination Chemistry Reviews*, vol. 500, Art. no. 215537, Feb. 2024, doi: 10.1016/j.ccr.2023.215537.

[29] M. A. Saraswati, W. H. Saputera, E. Lafina, and D. Sasongko, "Development of MnO2/γ-Al2O3 catalysts for catalytic ozonation of phenolic wastewater," *South African Journal of Chemical Engineering*, vol. 55, pp. 417–427, Jan. 2026, doi: 10.1016/j.sajce.2025.12. 009.

[30] A. Marin-Flores, E. M. Arce-Estrada, A. Romero-Serrano, A. Rivera-Benitez, J. López-Rodríguez, and A. Hernández-Ramírez, "Effect of the hydrothermal synthesis temperature on the capacitive performance of α-MnO2 particles," *International Journal of Electrochemical Science*, vol. 17, no. 10, Art. no. 221053, Oct. 2022, doi: 10.20964/2022.10. 48.

[31] Y. Kumar, S. Chopra, A. Gupta, Y. Kumar, S. J. Uke, and S. P. Mardikar, "Low temperature synthesis of MnO2 nanostructures for supercapacitor application," *Materials Science for Energy Technologies*, vol. 3, pp. 566–574, 2020, doi: 10.1016/j.mset.2020.06.002.

[32] V. L. Pham, D. G. Kim, and S. O. Ko, "Mechanisms of methylene blue degradation by nano-sized β-MnO2 particles," *KSCE Journal of Civil Engineering*, vol. 24, no. 5, pp. 1385–1394, May 2020, doi: 10.1007/s12205-020-2036-4.

[33] C. Agarwal and L. Csóka, "Developments in green nanotechnology: biogenic synthesis, mechanisms, applications," *Journal of Molecular Liquids*, vol. 446, Art. no. 129307, Mar. 2026, doi: 10.1016/j.molliq.2026.129307.

[34] R. Ahmed, K. H. Manik, M. S. Islam, A. Rhine, J. J. Mim, and N. Hossain, "Green synthesis methods for nanoparticles: Principles, biological routes, and physicochemical approaches toward sustainable nanotechnology," *Next Materials*, vol. 11, Art. no. 101929, 2026, doi: 10.1016/j. nxmate. 2026.101929.

[35] N. P. S. Chauhan et al., "Recent advances in the green synthesis of metal and metal oxide nanoparticles from plant extracts for biomedical and water remediation applications," *Next Nanotechnology*, vol. 9, Art. no. 100451, Jun. 2026, doi: 10.1016/j.nxnano.2026.100451.

[36] B. Nagaraj et al., "Anti-microbial and anti-cancer activity of gold nanoparticles phytofabricated using clerodin enriched clerodendrum ethanolic leaf extract," J*ournal of King Saud University - Science*, vol. 34, no. 4, Art. no. 101989, Jun. 2022, doi: 10.1016/j. jksus.2022.101989.

[37] S. Verma and R. Gupta, "Pharmacognostical and high performance thin layer chromatography studies on leaves of Clerodendrum infortunatum L.," *Ayu*, vol. 35, no. 4, pp. 416–422, Oct.–Dec. 2014, doi: 10.4103/0974-8520.159009.

[38] A. Kumar, R. Shukla, and A. Chaudhary, "Evaluation of antiulcerogenic activity of Clerodendron infortunatum extract on albino rat gastric ulceration: Antiulcer," *Journal of Drug Delivery and Therapeutics*, vol. 9, no. 4-A, pp. 57–62, Aug. 2019, doi: 10.22270/jddt.v9i4-A.3337.

[39] M. J. Uddin et al., "Phenylpropanoid and flavonoid glycosides from the leaves of Clerodendrum infortunatum (Lamiaceae)," *Biochemical Systematics and Ecology*, vol. 92, Art. no. 104131, Oct. 2020, doi: 10.1016/j.bse. 2020.104131.

[40] P. K. Sarkar et al., "Isolation and characterization of anti-diabetic compound from Clerodendrum infortunatum L. leaves," *South African Journal of Botany*, vol. 142, pp. 380–390, Nov. 2021, doi: 10.1016/j.sajb.2021. 06.0 40.

[41] S. Saha et al., "Formulation and chemical characterization of Clerodendrum infortunatum leaf extract in relation to anti-fungal activity," *Heliyon*, vol. 4, no. 12, Art. no. e01047, Dec. 2018, doi: 10.1016/j.heliyon.2018.e01047.

[42] A. Belcovici, D. Tocco, E. Fratini, A. Salis, and G. L. Turdean, "Composite material based on ZIF-8, reduced graphene oxide, and Nafion as electrode modifier for dopamine electrooxidation," *Microchemical Journal*, vol. 216, Art. no. 114769, Sep. 2025, doi: 10.1016/j.microc.2025. 114769.

[43] X. Fan, X. Xu, and P. Pintauro, "Performance and durability of fuel cell cathodes with a Nafion/FEP binder," *Journal of Power Sources*, vol. 664, Art. no. 238930, Feb. 2026, doi: 10.1016/j.jpowsour.2025.238930.

[44] J. Yang et al., "Insight into N2O formation over different crystal phases of MnO2 during low-temperature NH3–SCR of NO," *Catalysis Letters*, vol. 151, no. 10, pp. 2964–2971, Oct. 2021, doi: 10.1007/s10562-021-03541-8.

[45] A. M. Toufiq, F. Wang, Q. Javed, Q. Li, and Y. Li, "Photoluminescence spectra and magnetic properties of hydrothermally synthesized MnO2 nanorods," *Modern Physics Letters B*, vol. 27, no. 29, Art. no. 1350211, Nov. 2013, doi: 10.1142/S0217984913502114.